Creation and observation of topological magnetic monopoles and their interactions in a ferromagnetic meta-lattice

Arjun Rana
University of California Los Angeles
Chen-Ting Liao
University of Colorado Boulder https://orcid.org/0000-0002-3423-277X
Ezio Iacocca
University of Colorado Colorado Springs https://orcid.org/0000-0002-8870-5106
Ji Zou
University of California Los Angeles
Minh Pham
University of California Los Angeles
Xingyuan Lu
University of California Los Angeles
Emma-Elizabeth Cating Subramanian
University of Colorado
Yuan Hung Lo
University of California Los Angeles
Sinéad Ryan
University of Colorado
Charles Bevis
JILA, University of Colorado
Robert Karl Jr.
JILA, University of Colorado
Andrew Glaid
Penn State University
Jeffrey Rable
Penn State University
Pratibha Mahale
Penn State University
Joel Hirst
Sheffield Hallam University
Thomas Ostler

Sheffield Hallam University
William Liu
University of California, Los Angeles
Colum O'Leary
University of California, Los Angeles
Young-Sang Yu
Lawrence Berkeley National Laboratory
Karen Bustillo
Lawrence Berkeley National Lab https://orcid.org/0000-0002-2096-6078
Hendrik Ohldag
SLAC National Accelerator Laboratory https://orcid.org/0000-0002-2034-878X
David Shapiro
Lawrence Berkeley National Laboratory https://orcid.org/0000-0002-4186-6017
Sadegh Yazdi
Univ of colorado https://orcid.org/0000-0002-3470-9398
Thomas Mallouk
University of Pennsylvania
Stanley Osher
University of California, Los Angeles
Henry Kapteyn
Joint Institute for Laboratory Astrophysics
Vincent Crespi
Pennsylvania State University https://orcid.org/0000-0003-3846-3193
John Badding
Pennsylvania State University https://orcid.org/0000-0002-4517-830X
Yaroslav Tserkovnyak
University of California Los Angeles https://orcid.org/0000-0002-3277-3695
Margaret Murnane
JILA, University of Colorado Boulder
Jianwei (John) Miao (miao@physics.ucla.edu)
University of California Los Angeles https://orcid.org/0000-0003-4033-3945

Letter

Keywords:

Posted Date: March 10th, 2022

DOI: https://doi.org/10.21203/rs.3.rs-1413330/v1

Creation and observation of topological magnetic monopoles and their interactions in a ferromagnetic meta-lattice

Arjun Rana[1,2*], Chen-Ting Liao[2,3*], Ezio Iacocca[4,5], Ji Zou[1], Minh Pham[2,6], Xingyuan Lu[1,7], Emma-Elizabeth Cating Subramanian[2,3], Yuan Hung Lo[1,2], Sinéad A. Ryan[2,3], Charles S. Bevis[2,3], Robert M. Karl Jr[2,3], Andrew J. Glaid[8], Jeffrey Rable[8], Pratibha Mahale[8,9], Joel Hirst[10], Thomas Ostler[10,11], William Liu[1,2], Colum M. O'Leary[1,2], Young-Sang Yu[12], Karen Bustillo[13], Hendrik Ohldag[12], David A. Shapiro[12], Sadegh Yazdi[14], Thomas E. Mallouk[8,9], Stanley J. Osher[2,6], Henry C. Kapteyn[2,3], Vincent H. Crespi[8], John V. Badding[8], Yaroslav Tserkovnyak[1], Margaret M. Murnane[2,3], Jianwei Miao[1,2]

[1]Department of Physics & Astronomy and California NanoSystems Institute, University of California, Los Angeles, CA 90095, USA. [2]STROBE Science and Technology Center. [3]JILA and Department of Physics, University of Colorado and NIST, 440 UCB, Boulder, Colorado 80309, USA. [4]Department of Mathematics, Physics, and Electrical Engineering, Northumbria University, Newcastle upon Tyne, NE1 8ST, UK. [5]Center for Magnetism and Magnetic Materials, University of Colorado, Colorado Springs, CO 80918, USA. [6]Department of Mathematics, University of California, Los Angeles, CA 90095, USA. [7]School of Physical Science and Technology, Soochow University, Suzhou 215006, China. [8]Departments of Chemistry, Physics, Materials Science and Engineering and Materials Research Institute, Penn State University, University Park, PA 16802, USA. [9]Department of Chemistry, University of Pennsylvania, Philadelphia PA 19104, USA. [10]Materials and Engineering Research Institute, Sheffield Hallam University, Howard Street, Sheffield S1 1WB, UK. [11]Department of Engineering and Mathematics, Sheffield Hallam University, Howard Street, Sheffield S1 1WB, UK. [12]Advanced Light Source, Lawrence Berkeley National Laboratory, Berkeley, CA 94720, USA. [13]National Center for Electron Microscopy, Molecular Foundry, Lawrence Berkeley

National Laboratory, Berkeley, CA, 94720, USA. [14]*Renewable and Sustainable Energy Institute, University of Colorado, Boulder, CO 80309, USA.*

[*]*These authors contributed equally to this work.*

Topological magnetic monopoles, also known as hedgehogs or Bloch points, are three-dimensional (3D) nonlocal spin textures that are robust to thermal and quantum fluctuations due to their topology[1-4]. Understanding their properties is of both fundamental interest and practical applications[1-9]. However, it has been difficult to experimentally produce topological magnetic monopoles in a controlled manner and directly observe their 3D magnetization vector field and interactions at the nanoscale. Here, we report the creation of 138 stable topological magnetic monopoles at the specific sites of a ferromagnetic meta-lattice at room temperature. We further develop 3D soft x-ray vector ptychography to determine the magnetization vector and emergent magnetic field of the topological monopoles with a 3D spatial resolution of 10 nm. This spatial resolution is comparable to the magnetic exchange length of transition metals[10], enabling us to probe monopole-monopole interactions. We find that the topological monopole pairs with positive and negative charges are separated by 18.3±1.6 nm, while the positively and negatively charged pairs are stabilized at comparatively longer distances of 36.1±2.4 nm and 43.1±2.0 nm, respectively. We also observe virtual topological monopoles created by magnetic voids in the meta-lattice. This work demonstrates that ferromagnetic meta-lattices could be used as a new platform to create and investigate the interactions and dynamics of topological magnetic monopoles. Furthermore, we expect that soft x-ray vector ptychography can be broadly applied to quantitatively image 3D vector fields in magnetic and anisotropic materials at the nanoscale.

The 3D ferromagnetic meta-lattice was synthesized by self-assembly of a face-centred cubic template using silica nanospheres of 60 nm in diameter (Methods). The interstitial spaces between the nanospheres of the template were infiltrated with nickel to create a meta-lattice, comprising octahedral and tetrahedral sites interconnected by thin necks[11,12]. Superconducting quantum interference device measurements show that the saturation magnetization of the meta-lattice is consistent with that of the nickel thin film (Extended Data Fig. 1). The complex 3D curved surfaces of the silica nanospheres in the meta-lattice creates a magnetically frustrated configuration that harbours topological spin textures. To quantitatively characterize the topological spin textures, we developed 3D soft x-ray vector ptychography for the simultaneous determination of the electron density and the magnetization vector field without requiring any prior knowledge of the sample. This represents a significant advantage over previous methods that either rely on *a priori* assumptions[13] or use Maxwell's equations as a constraint[14-16] to image the 3D vector field. Furthermore, by taking advantage of the high differential magnetic contrast at the L_3-edge resonance of transition metals[13,17], we demonstrated soft x-ray vector ptychography with a 3D spatial resolution of 10 nm, which is close to the magnetic exchange length of transition metals[10] and an order of magnitude higher than that of hard x-ray vector tomography[2,9].

The experiment was conducted by focusing circularly polarized soft x-rays onto the ferromagnetic meta-lattice (Fig. 1). The magnetic contrast of the sample was obtained by using x-ray magnetic circular dichroism[13,17,18] and tuning the x-ray energy to the L_3-edge of nickel[19]. To separate the magnetic contrast from the electron density, two independent measurements were made with left- and right-circularly polarized soft x-rays. In each measurement, three independent tilt series were acquired from the sample, corresponding to three in-plane rotation angles (0°, 120° and 240°) around the z-axis (Fig. 1 and Extended Data Fig. 2). Each tilt series was collected by rotating the sample around the x-axis with a tilt range from -62° to +61°. At each tilt angle, a focused x-ray beam was scanned over the sample with partial overlap between adjacent scan positions and a far-field diffraction pattern was recorded by a charge-coupled device camera at each scan position (Methods). The full data set consists of six tilt series with a total of 796,485 diffraction patterns.

The diffraction patterns were reconstructed using a regularized ptychographic iterative engine[20], where corrupted diffraction patterns were removed and phase unwrapping was implemented (Methods, Extended Data Fig. 3). Each pair of left- and right-circularly polarized projections was aligned and converted to the optical density for normalization. The sum of each pair of the oppositely polarized projections produced three independent tilt series corresponding to three in-plane rotation angles. The scalar tomographic reconstruction was performed from the three tilt series of 91 projections using a real space iterative algorithm (Methods), which can optimize the reconstruction by iteratively refining the spatial and angular alignment of the projections. Quantitative characterization of the reconstructed 3D electron density and a scanning transmission electron microscopy image of the sample indicates that, although there are some imperfections, the meta-lattice has an ordered face-centred cubic structure (Extended Data Figs. 4 and 5a, b). To determine the magnetization vector field, we took the difference of the left- and right-circularly polarized projections of the three tilt series (Extended Data Fig. 6). The 3D vector reconstruction was performed from 91 difference projections by least-squares optimization with gradient descent (Methods). Supplementary Video 1 shows the 3D electron density and magnetization vector field of the ferromagnetic meta-lattice. To validate the 3D vector reconstruction and quantify the spatial resolution, we divided all the projections into two halves by choosing alternate projections and performed two independent 3D vector reconstructions. By calculating the Fourier shell correlation from the two independent reconstructions, we quantified that a spatial resolution of 10 nm was achieved for the 3D vector reconstruction of the magnetization field (Methods and Extended Data Fig. 7).

Next, we applied topological theory[21] to quantitatively analyse the experimental 3D magnetization vector field and identify nonlocal spin textures. In 3D magnetic systems, a topological magnetic monopole within a bulk Ω follows the bulk-surface relationship[4] (i.e., the divergence theorem),

$$Q = \int_{\Omega} \rho \, dxdydz = \int_{\partial\Omega} \boldsymbol{B}_e \cdot d\boldsymbol{S}\,, \qquad (1)$$

where Q is the topological charge with the charge density $\rho = \frac{3}{4\pi} \partial_x \boldsymbol{n} \cdot \left(\partial_y \boldsymbol{n} \times \partial_z \boldsymbol{n}\right)$, $\partial\Omega$ is the bounding surface, $\boldsymbol{n}$ is the normalized magnetization vector field, $B_e^i = \frac{1}{8\pi} \epsilon^{ijk} \boldsymbol{n} \cdot \left(\partial_j \boldsymbol{n} \times \partial_k \boldsymbol{n}\right)$ is the emergent magnetic field, and ϵ^{ijk} is the Levi-Civita symbol. $\boldsymbol{B}_e$ acts on (quasi)particles such as electrons and magnons moving through the magnetic texture as long as they carry a spin[3]. The right-hand side of Eq. (1) is commonly used to evaluate the skyrmion number in a 2D plane[22,23], but can be generalized to any 3D embedded surface. When the magnetization vector on the surface of a sphere enclosing a volume Ω covers the orientational parameter space exactly once, we have the topological charge $Q = \pm 1$, where +1 and -1 represent positively and negatively charged monopoles, respectively. It is important to note that skyrmions and topological magnetic monopoles are fundamentally different spin textures. Skyrmions are local textures and can be annihilated by shrinking their cores down to the lattice constant without affecting the spin states far away[22,23]. In contrast, topological magnetic monopoles are nonlocal spin textures and robust to local fluctuations[1-4]. They are topologically conserved, i.e. the bulk-surface relationship of equation (1), even when the system is not well-ordered. Topological monopoles can only be removed by the outflow of a topological current through the boundary or annihilated in pairs of opposite-charged monopoles.

Although we used the normalized magnetization vector field ($\boldsymbol{n}$) in this study, equation (1) holds even when $\boldsymbol{n}$ varies in its magnitude[4]. To apply equation (1) to the meta-lattice, we computed the local maxima and minima of the topological charge density within the bulk of the sample. At each local extremum, we defined an enclosed surface and calculated the topological charge (Methods). Figure 2a and Supplementary Video 2 show the 3D spatial distribution of 68 and 70 topological magnetic monopoles with positive (red dots) and negative (blue dots) charges in the meta-lattice. Although there are twice as many tetrahedral than octahedral sites in the meta-lattice, we found that more magnetic monopoles exist in the octahedral than the tetrahedral sites (Extended Data Table 1). Figure 2b and d show two representative topological magnetic monopoles with a positive and negative charge located in an octahedral and tetrahedral site, respectively. The 3D magnetization vector field of the topological magnetic monopoles is shown in Fig. 2c and e. The sign of the charge is not apparent from the 3D magnetization vector field, but can be unambiguously observed from the emergent magnetic field (Extended Data Fig. 8a and b).

The existence of a large number of topological magnetic monopoles in the ferromagnetic meta-lattice allowed us to investigate their interactions. According to monopole confinement theory[4], the potential energy of a monopole pair with a positive and negative charge grows linearly with their separation when the exchange energy dominates, with all the emergent magnetic field lines emanating from the positive charge and ending at the negative charge. A non-negligible pair separation indicates the existence of other interactions competing with the exchange energy. Figure 3a shows a representative topological monopole pair with a positive and negative charge, where the emergent magnetic field lines were computed from the magnetization vector field using Eq. (1). We observed that only part of the magnetic flux emanating from the positive charge terminates at the negative charge, indicating that the emergent magnetic field lines are not completely confined. In comparison, the emergent magnetic field lines in similarly charged pairs exhibit repulsive interactions (Fig. 3b and c). The distance of the topological magnetic monopole pairs with positive and negative charges was fit to be 18.3 ± 1.6 nm (Fig. 3d), while the positively and a negatively charged pairs were stabilized at longer distances of 36.1 ± 2.4 nm and 43.1 ± 2.0 nm (Fig. 3e and f), respectively. The statistically significant difference in the nearest-neighbour distance between oppositely and similarly charged magnetic monopoles is consistent with theory[4]. To examine if the imperfections in the sample affect the interactions of the topological magnetic monopoles, we chose a more ordered region in the meta-lattice and plotted the histogram of the nearest-neighbour distance between oppositely and similarly charged magnetic monopoles in the region (Extended Data Fig. 5), which agrees with that obtained from a larger region including some imperfections (Fig. 3d-f). The consistency of the two histograms confirms that the structural imperfections in the meta-lattice do not play a significant role in influencing the interactions of the topological magnetic monopoles.

According to the bulk-surface relationship of equation (1), the topological charge can be computed on an arbitrary surface. In the meta-lattice, the silica nanospheres are magnetic voids and create 3D internal surfaces within the ferromagnetic network. To calculate the topological charge on these 3D surfaces, we performed a non-convex triangulation of the internal structure of the meta-lattice. The resulting facets were grouped into individual void surfaces by a community-clustering technique used in network analysis[24]. In accordance with the literature[25], we defined any void surface with $|Q| \geq 0.9$ as a virtual topological magnetic monopole. Figure 2a and Supplementary Video 2 show the distribution of 8 and 11 virtual topological monopoles with positive (red surface) and negative charges (blue surface) in the ferromagnetic meta-lattice. Two representative virtual topological monopoles with $Q = 1.01$ and -1 are shown in Fig. 4a and b, respectively. The 3D magnetization vector field on the two magnetic voids was mapped onto a 2D plane to produce two stereographic projections, exhibiting skyrmion and antiskyrmion configurations (Fig. 4c and d). For the virtual topological monopole with a positive charge, most spins point down in the centre and up at the boundary, while for the virtual monopole with a negative charge, most spins point up in the centre and down at the boundary. The emergent magnetic field of the virtual topological monopoles (Extended Data Fig. 8c and d) shows features as if real topological monopoles reside at the geometric centres of the magnetic voids, which is a clear manifestation of the bulk-surface correspondence.

Compared to materials systems that usually support topological defects, such as non-centrosymmetric lattices and magnetic / heavy-metal multilayers[1,22,23], the ferromagnetic meta-lattice studied does not possess strong anisotropy or the Dzyaloshinskii-Moriya interaction. However, surface curvature can stabilize magnetic solitons through the effective Dzyaloshinskii-Moriya interaction[26,27]. The complex 3D curved surface of the magnetic voids induces strong magnetostatic frustration in the ferromagnetic meta-lattice, which harbours topological magnetic monopoles at the octahedral and tetrahedral sites of the lattice and the associated skyrmion textures on the surface of the magnetic voids. Using our experimental data as direct input to atomistic simulations, we numerically demonstrated that topological magnetic monopoles can be stabilized by the boundary conditions (Methods). We extracted four $15\times15\times15$ nm^3 volumes from the ferromagnetic meta-lattice, containing four topological magnetic monopoles with two positive and two negative charges. The atomistic spins on the outer boundary of each volume were fixed, while all the other spins were allowed to relax to an equilibrium configuration. After 50 ps, a stable magnetic monopole formed in each volume with a topological charge matching the experimental value (Extended Data Fig. 9a-d). We also observed that as long as the atomistic spins were fixed on four of the six surfaces of each volume, the topological magnetic monopole remained stable inside the volume (Extended Data Fig. 9e-h). These results further confirm that surface constraints can stabilize topological magnetic monopoles.

In conclusion, we have created and directly observed topological magnetic monopoles and their interactions in a ferromagnetic meta-lattice with a 3D spatial resolution of 10 nm. This work could open the door to use magnetically frustrated meta-lattices as a new platform to study the interactions, dynamics, and confinement-deconfinement transition of topological monopoles[4]. Furthermore, as a powerful scanning coherent diffractive imaging method[28-31], the 3D spatial resolution of soft x-ray vector ptychography can be improved by increasing the incident coherent flux or the data acquisition time. With the rapid development of advanced synchrotron radiation, x-ray free electron lasers and high harmonic generation sources worldwide[29], we expect that 3D vector ptychography can find broad applications in the topological spin texture, nanomagnetism and x-ray imaging fields.

References

1. Milde, P. et al. Unwinding of a skyrmion lattice by magnetic monopoles. *Science* **340**, 1076–1080 (2013).
2. Donnelly, C. et al. Three-dimensional magnetization structures revealed with X-ray vector nanotomography. *Nature* **547**, 328–331 (2017).
3. Tatara, G. & Nakabayashi, N. Emergent spin electromagnetism induced by magnetization textures in the presence of spin-orbit interaction. *J. Appl. Phys.* **115**, 172609 (2014).
4. Zou, J., Zhang, S. & Tserkovnyak, Y. Topological transport of deconfined hedgehogs in magnets. *Phys. Rev. Lett.* **125**, 267201 (2020).
5. Pietilä, V & Möttönen, M. Creation of Dirac monopoles in spinor Bose-Einstein condensates. *Phys. Rev. Lett*. **103**, 030401 (2009).
6. Ray, M. W., Ruokokoski, E., Kandel, S., Möttönen, M. & Hall, D. S. Observation of Dirac monopoles in a synthetic magnetic field. *Nature* **505**, 657–660 (2014).
7. Im, M.-Y. et al. Dynamics of the Bloch point in an asymmetric permalloy disk. *Nat. Commun.* **10**, 593 (2019).
8. Yu, X. et al. Real-Space Observation of Topological Defects in Extended Skyrmion-Strings. *Nano Lett.* **20**, 7313–7320 (2020).
9. Donnelly, C. et al. Experimental observation of vortex rings in a bulk magnet. *Nat. Phys*. **17**, 316–321 (2021).
10. Abo, G. S. et al. Definition of Magnetic Exchange Length. *IEEE Trans. Magn*. **49**, 4937-4939 (2013).

11. Han, J. E. & Crespi, V. H. Abrupt Topological Transitions in the Hysteresis Curves of Ferromagnetic Metalattices. *Phys. Rev. Lett* . **89**, 197203 (2002).

12. Liu, Y. *et al.* Confined chemical fluid deposition of ferromagnetic metalattices. *Nano Lett.* **18**, 546–552 (2018).

13. Streubel, R. *et al.* Retrieving spin textures on curved magnetic thin films with full-field soft X-ray microscopies. *Nat. Commun.* **6**, 1–11 (2015).

14. Phatak, C., Petford-Long, A. K. & De Graef, M. Three-dimensional study of the vector potential of magnetic structures. *Phys. Rev. Lett*. **104**, 253901 (2010).

15. Phatak, C. , Heinonen, O., De Graef, M. & Petford-Long, A. K. Nanoscale skyrmions in a nonchiral metallic multiferroic: Ni_2MnGa. *Nano Lett*. **16**, 4141–4148 (2016).

16. Davis, T. J., Janoschka, D., Dreher, P. & Frank, B. Ultrafast vector imaging of plasmonic skyrmion dynamics with deep subwavelength resolution. *Science* **368**, eaba6415 (2020).

17. Stöhr, J. & Siegmann, H. C. *Magnetism: From Fundamentals to Nanoscale Dynamics* 1st edn (Springer, 2006).

18. Tripathi, A. *et al*. Dichroic coherent diffractive imaging. *Proc. Natl. Acad. Sci. USA* **108**, 13393–13398 (2011).

19. Chen, C. T., Sette, F., Ma, Y. & Modesti, S. Soft-x-ray magnetic circular dichroism at the $L_{2,3}$ edges of nickel. *Phys. Rev. B* **42**, 7262-7265 (1990).

20. Maiden, A., Johnson, D. & Li, P. Further improvements to the ptychographical iterative engine. *Optica* **4**, 736–745 (2017).

21. Nakahara, M. *Geometry, Topology and Physics* 2nd edn (New York: Tailor & Francis, 2003).

22. Nagaosa, N. & Tokura, Y. Topological properties and dynamics of magnetic skyrmions. *Nat. Nanotechnol.* **8**, 899–911 (2013).

23. Fert, A., Reyren, N. & Cros, V. Magnetic skyrmions: advances in physics and potential applications. *Nat. Rev. Mater.* **2**, 1–15 (2017).

24. Jain, A. K., Murty, M. N. & Flynn, P. J. Data clustering: a review. *ACM Comput. Surv.* **31**, 264–323 (1999).

25. Cortés-Ortuño, D. *et al.* Nanoscale magnetic skyrmions and target states in confined

geometries. *Phys. Rev. B* **99**, 214408 (2019).

26. Streubel, R. *et al.* Magnetism in curved geometries. *J. Phys. D. Appl. Phys.* **49**, 363001 (2016).
27. Vitelli, V. & Turner, A. M. Anomalous coupling between topological defects and curvature. *Phys. Rev. Lett.* **93**, 215301 (2004).
28. Miao, J., Charalambous, P., Kirz, J. & Sayre, D. Extending the methodology of X-ray crystallography to allow imaging of micrometre-sized non-crystalline specimens. *Nature* **400**, 342 (1999).
29. Miao, J., Ishikawa, T., Robinson, I. K. & Murnane, M. Beyond crystallography: Diffractive imaging using coherent x-ray light sources. *Science* **348**, 530-535 (2015).
30. Rodenburg, J. M. *et al.* Hard-x-ray lensless imaging of extended objects. *Phys. Rev. Lett.* **98**, 34801 (2007).
31. Thibault, P. *et al*. High-Resolution Scanning X-ray Diffraction Microscopy. *Science* **321**, 379–382 (2008).

Figures and figure legends

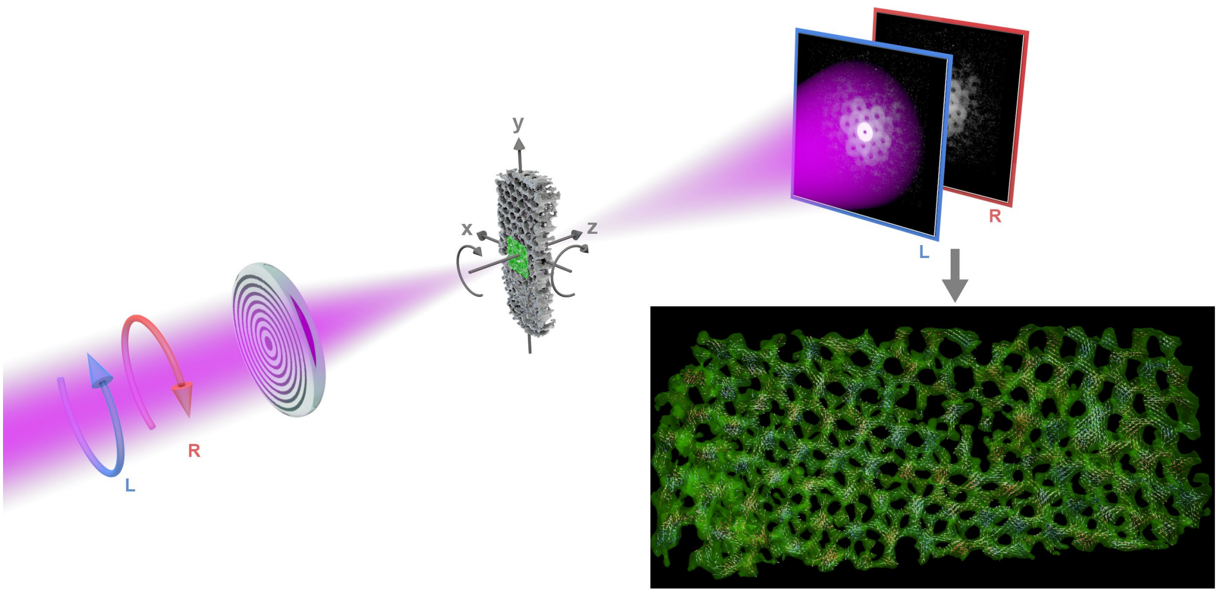

Fig. 1. Experimental schematic of 3D soft x-ray vector ptychography. Left- and right-circularly polarized x-rays (pink) were focused onto a ferromagnetic meta-lattice sample (centre), on which the green circles indicate the partially overlapped scan positions. The sample was titled around the x- and z-axis and diffraction patterns were collected by a charge-coupled

device camera. The lower right structure shows the 3D electron density (green) and magnetization vector field (arrows) of the meta-lattice reconstructed from the diffraction patterns.

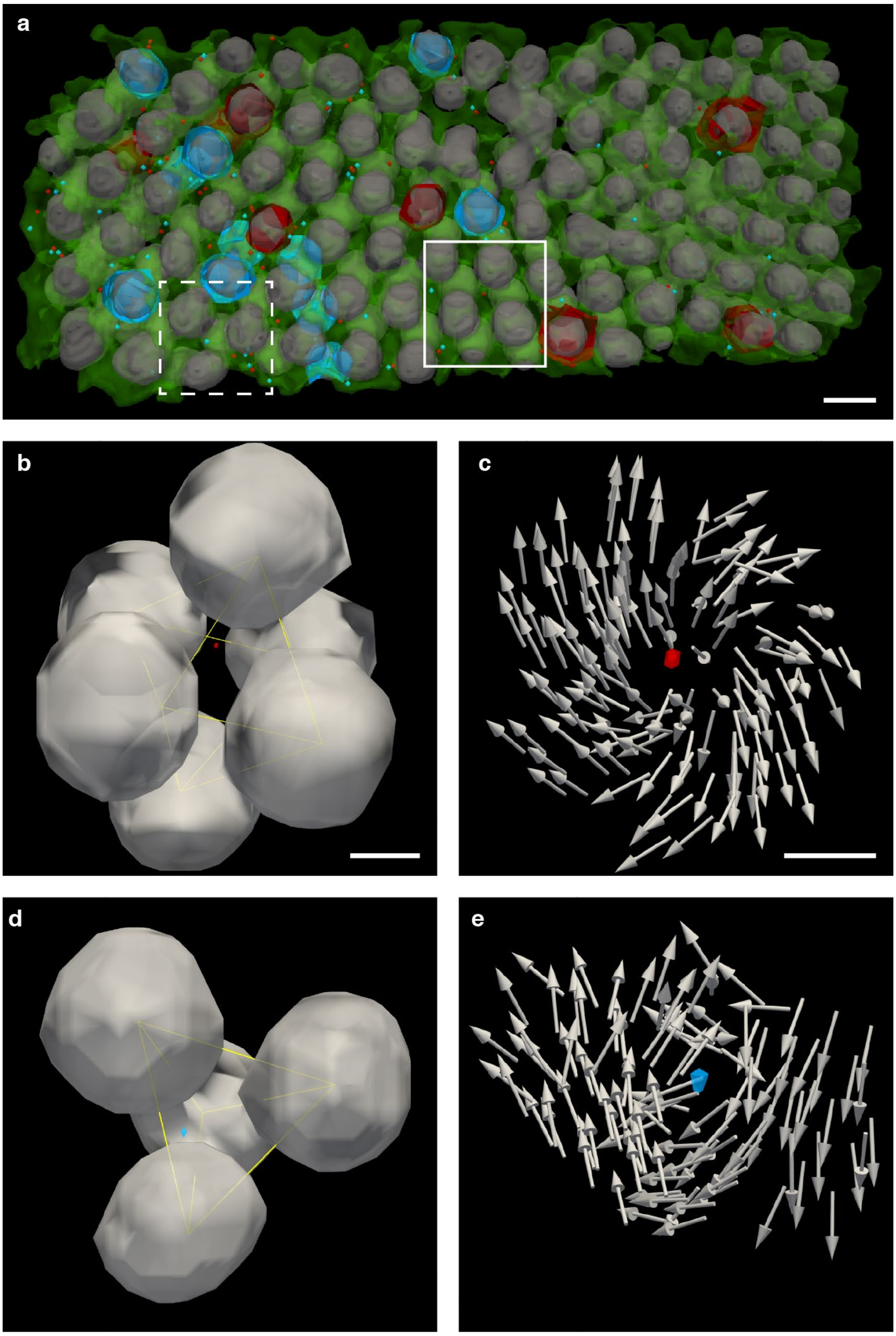

Fig. 2. Quantitative 3D characterization of topological magnetic monopoles in the

ferromagnetic meta-lattice. a, 3D spatial distribution of 68 and 70 topological monopoles with positive (red dots) and negative charges (blue dots) in the meta-lattice, where the surfaces of the magnetic voids in red and blue represent virtual topological monopoles with positive and negative charges, respectively. The solid and dashed squares mark the region of interest shown in (**b**) and (**d**), respectively. **b, c**, The location and 3D spin textures of a positively charged topological monopole within a tetrahedral site of the face-cantered cubic meta-lattice. **d, e**, The location and 3D spin textures of a negatively charged topological monopole within an octahedral site. Scale bars, 60 nm (**a**); 25 nm (**b**); and 10 nm (**c**).

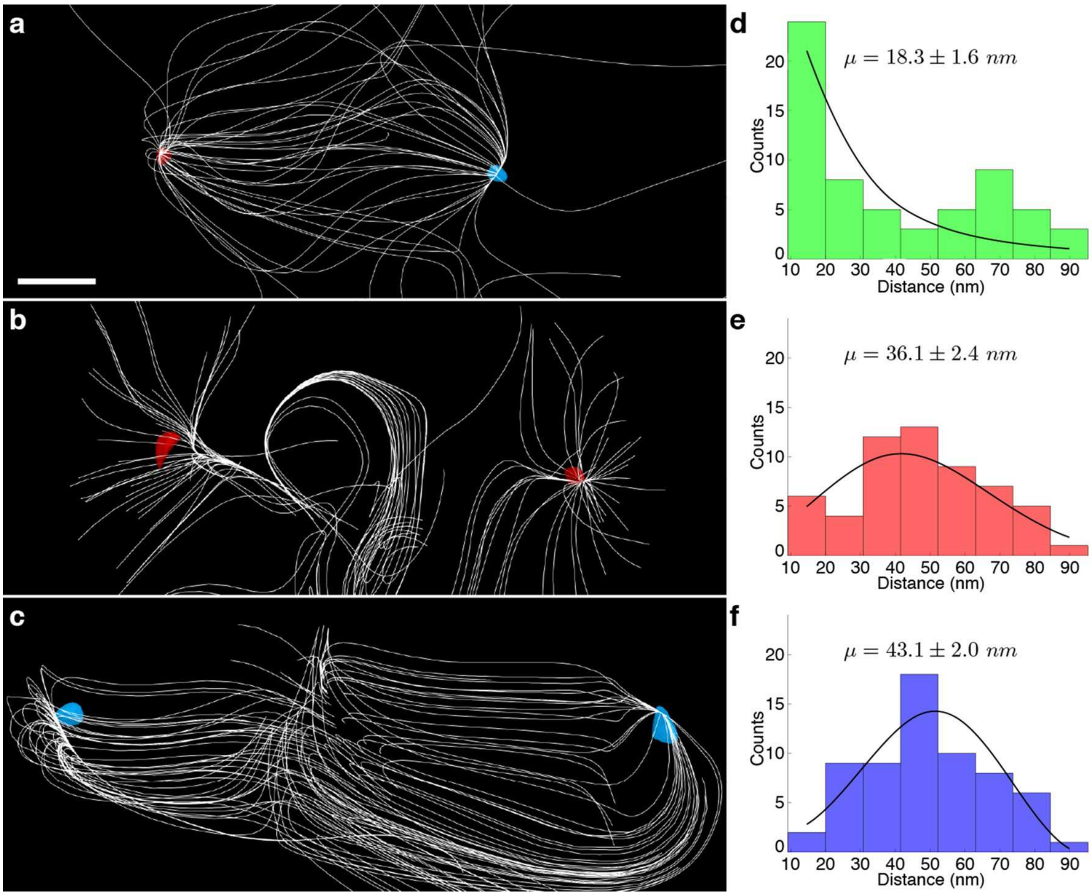

Fig. 3. Interactions of the topological magnetic monopoles in the ferromagnetic meta-lattice. a-c, Three representative topological monopole pairs with a positive and negative charge (**a**), two positive (**b**) and two negative charges (**c**), where the white lines represent the emergent magnetic field lines. **d-f**, Histograms of the nearest-neighbour distance for the topological monopole pairs with a positive and negative charge (**d**), two positive (**e**) and two

negative charges (**f**). The three histograms were fit to a generalized extreme value distribution, producing three curves in (**d-f**), where μ represents the centre of each fit and the standard error was determined from the fit's confidence interval. Scale bar, 5 nm.

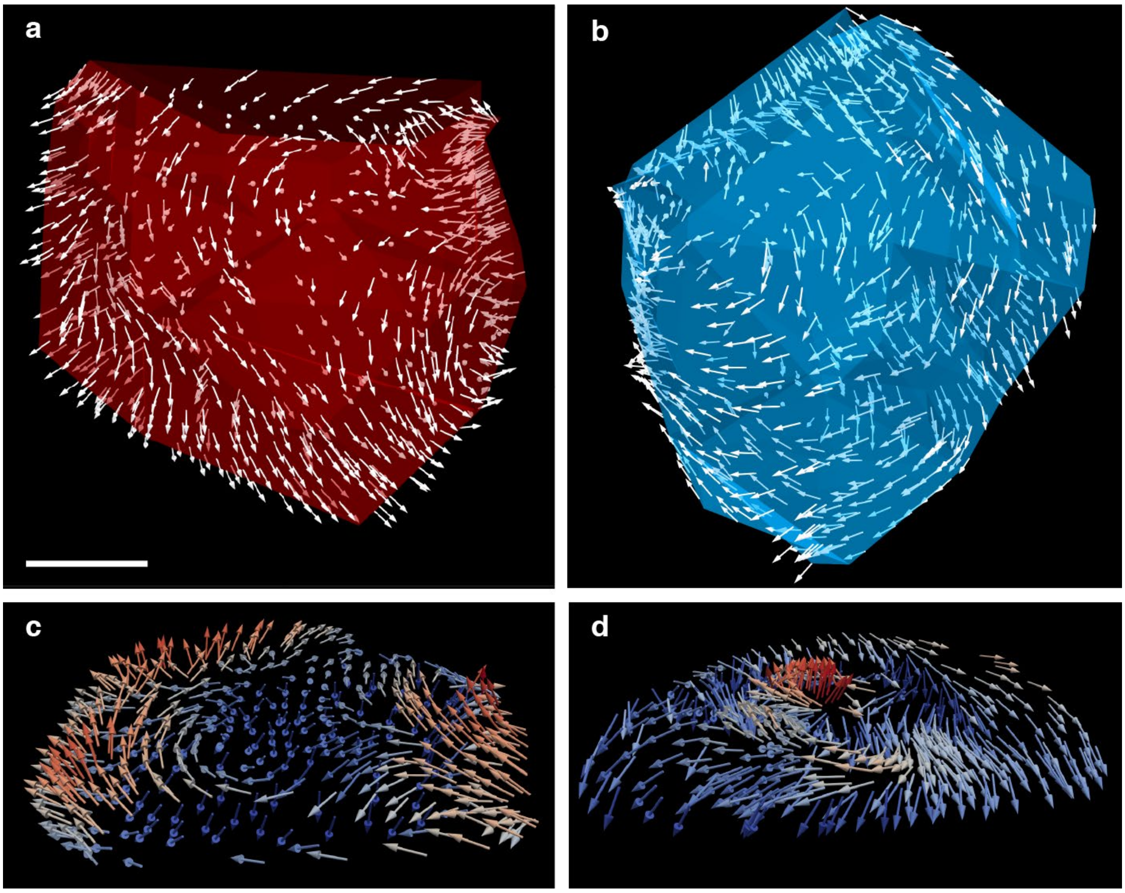

Fig. 4. Representative virtual topological monopoles in the ferromagnetic meta-lattice. a, b, Two virtual topological monopoles with $Q = 1.01$ and -1, respectively, where the arrows indicate the 3D magnetization vector field. **c, d,** Stereographic projections of the virtual topological monopoles shown in (**a**) and (**b**), respectively, where the colours of the arrows represents the z-component of the spin with pointing up (+z) in red and down (-z) in blue. Scale bar, 15 nm.

METHODS

Sample synthesis and preparation. The 3D ferromagnetic meta-lattice was synthesized by infiltrating interconnected voids of a silica nanoparticle template using confined chemical fluid deposition[12]. Monodisperse silica nanoparticles of 60 nm in diameter (standard deviation < 5%) were synthesized using a liquid-phase method[32]. The evaporation-assisted vertical deposition technique was used to assemble these particles onto silicon substrate[33]. Briefly, 3 cm x 1 cm silicon wafers were placed at a ~30° angle in open plastic vials containing 10x dilute solution of the as-synthesized particles. The vials were left undisturbed for two weeks in an oven maintained at 40° C at 80% relative humidity. The resulting films that were used as the template for nickel infiltration contained silica particles arranged in a face-centred cubic structure and had thicknesses ranging from 240 nm – 850 nm depending on the vertical position of the silicon substrate[34].

The infiltration of nickel within the template voids was performed using confined chemical fluid deposition[12]. The template was spatially confined using a 250 µm thick U-shaped titanium spacer and placed within a custom-built reactor made of parts from High Pressure Equipment Company, McMaster, and Swagelok. Bis(cyclopentadienyl) nickel (II) was loaded into the reactor in a Vacuum Atmospheres argon glovebox. The reactor was pressurized with Praxair 4.0 Industrial Grade carbon dioxide using a custom-made manual pump and heated to 70°C for 8 hours at a pressure of around 13.8 MPa to dissolve the precursor powder into the supercritical carbon dioxide. A separate gas reservoir was loaded with Praxair 5.0 ultra-high purity hydrogen using a Newport Scientific Two Stage 207 MPa Diaphragm Pump and was connected to the reactor. The hydrogen was added to the reactor to a final reactor pressure of 42.7 MPa and the deposition proceeded at 100°C for 10 hours. The interstitial voids between the nanospheres of the template were then infiltrated with nickel, forming a meta-lattice. An overfilled nickel film over the meta-lattice and template resulting from the deposition process was milled using a Leica EM TIC 3x Argon ion beam milling system at 3 degrees and 3 kV.

To prepare the sample with the correct geometry for the 3D vector ptychography experiment, we lifted out a portion of the sample from the bulk meta-lattice on a silicon substrate and thinned the sample using a focused ion beam (FIB, FEI Nova 600 NanoLab DualBeam), which was equipped with a field emission scanning electron microscope and a scanning gallium ion beam. The FIB prepared sample was mounted on a 3-mm TEM grid (Omniprobe, 3 posts copper lift-out grid), where the central post was also trimmed by FIB milling to increase the tilt range. The sample mounted on the TEM grid was examined by the scanning electron microscope and an optical microscope, and then manually glued on a 3-mm copper ring using a silver paste (Extended Data Fig. 2a-f). The sample fabricated by this process can be manually rotated in-plane for the 3D vector ptychography experiment. To examine the surface oxidation of the sample, we conducted an x-ray absorption spectroscopy experiment of the Ni meta-lattice. By carefully analysing the x-ray absorption spectrum in comparison with that of a pure Ni film and a NiO film[35] (Extended Data Fig. 2g), we concluded that the surface oxide layer of the sample is very thin, which is consistent with the previous experimental measurements[36].

The 3D soft x-ray vector ptychography experiment. The experiment was conducted at the COSMIC beam line at the Advanced Light Source, Lawrence Berkeley National Lab[37]. Figure 1 shows the experimental schematic of 3D soft x-ray vector ptychography. An elliptical polarization undulator was used to generated circularly polarized x-rays of left- and right-helicity and achieve differential contrast enhancement of the magnetic signal. The incident photon energy was tuned to 856 eV, slightly above the nickel L_3 edge, to obtain the magnetic contrast based on x-ray magnetic circular dichroism[13,17-19,38]. The polarized beam was focused onto the sample by a Fresnel zone plate with an outer width of 45 nm. A total of six tilt series with a tilt range from -62° to +61° were acquired from the sample with left- and right-circularly polarized x-rays at three in-plane rotation angles (0°, 120° and 240°). At each tilt angle, the focused beam was raster-scanned across the sample in 40 nm steps. Diffraction patterns were collected using both left- and right-circularly polarized x-rays. A charge-coupled device camera was used to record the diffraction patterns at each scan position. Initial reconstructions were performed on-site in real time using a

GPU-based ptychography reconstruction algorithm[39].

Data processing and ptychographic reconstructions. A very small number of corrupted diffraction patterns, most commonly caused by detector readout malfunction or unstable beam flux, resulted in a global degradation of the reconstruction through the coupling of the probe and object. We used the following procedure to automatically detect and remove the corrupted diffraction patterns to achieve the high-quality reconstruction. The high-angle diffraction intensity at each scan position was integrated to produce a low-resolution map at every ptychography scan. Local maxima in the magnitude of the gradient of this map were used to identify and remove bad frames (Extended Data Fig. 3a and b). The image reconstructions were performed by using the regularized ptychographic iterative engine[20] coupled with phase unwrapping for high tilt angles[40] (Extended Data Fig. 3c and d). Specifically, for the first 10 iterations of the ptychographic reconstruction, no phase unwrapping was enforced. After that, phase unwrapping was applied to the object in every 3rd iteration[40]. The final reconstruction was obtained with a total of 500 iterations.

From the reconstructed complex-valued exit wave, the absorption component was used as the magnetic contrast[17,18] and the two oppositely-polarized projections at each tilt angle were aligned using a feature-based image registration package in MATLAB. The projections were converted to optical density[41] to normalize any small temporal and polarization-based fluctuations of the beam intensity. In each projection, background subtraction was performed by numerically evaluating Laplace's equation,

$$\nabla^2 \varphi = 0 \quad , \qquad (2)$$

where $\nabla^2 = \frac{\partial^2}{\partial x^2} + \frac{\partial^2}{\partial y^2}$ is the 2D Laplace operator and φ represents the background of the projection. To determine φ we solved equation (2) by using the region exterior to the sample as the boundary condition. The value at the boundary corresponds to the optical density in vacuum. Mathematically, the calculation of φ is equivalent to the determination of the geometry of a soap film from an enclosed boundary. We implemented this procedure by using a MATLAB function called 'regionfill'. We found that this method outperforms simple constant background subtraction by taking into account the local variation of the background[42].

The scalar tomography reconstruction. The relationship between charge and magnetic scattering[17,18,43],

$$f = f^c \pm i f^m \, \hat{z} \cdot \boldsymbol{m} \ , \qquad (3)$$

was used to generate a set of scalar and vector projections corresponding to the charge and magnetic scattering, where f^c and f^m are the charge and magnetic scattering factor, respectively, $\hat{z}$ is the x-ray propagation direction, and $\boldsymbol{m}$ is the magnetization vector. The sum of each pair of the oppositely-polarized projections produced three independent tilt series corresponding to three in-plane rotation angles. The scalar projections of each tilt series were first roughly aligned with cross-correlation, then more accurately aligned using the centre-of-mass and common line method[44]. The aligned tilt series was reconstructed by a real space iterative reconstruction (RESIRE) algorithm[42,45], which was able to iteratively perform angular and spatial refinement to adjust any remaining small alignment errors. From the three independent reconstructions, transformation matrices were computed to align the three tilt series to a global coordinate system. The three aligned tilt series were collectively reconstructed by RESIRE using the same angular and spatial refinement procedure, which produced the final scalar tomography reconstruction. The transformation matrices obtained from the scalar tomography were used for the vector tomography reconstruction.

The vector tomography reconstruction. The 3D vector magnetization field was reconstructed by taking the difference of the left- and right-circularly polarized projections of the six experimental tilt series, producing three independent tilt series with the magnetic contrast. The vector tomography algorithm is modelled as a least squares optimization problem and solved directly by gradient descent. The least squares problem is given as,

$$min_{O_1,O_2,O_3}\, f(O_1,O_2,O_3) \;= \sum_{i=1}^{N} ||\,\alpha_i \Pi_i O_1 + \beta_i \Pi_i O_2 + \gamma_i \Pi_i O_3 - b_i||^2$$

$$= \sum_{i=1}^{N} ||\,\Pi_i(\alpha_i O_1 + \beta_i O_2 + \gamma_i O_3) - b_i||^2 \quad , \qquad (4)$$

where O_1, O_2, O_3 are the three components of the vector field to be reconstructed, N is the number of the projections of the three tilt series, Π_i is the projection operator with respect to the Euler angle set $\{\phi_i, \theta_i, \psi_i\}$, and b_i is the experimentally measured projection. $\{\alpha_i, \beta_i, \gamma_i\}$ are the coefficient set with respect to the projection operator and are related to the corresponding Euler angle set by,

$$\alpha_i = sin\,\theta_i\, cos\,\phi_i, \quad \beta_i = sin\,\theta_i\, sin\,\phi_i, \quad \alpha_i = cos\,\theta_i \quad . \qquad (5)$$

The least square problem is solved via gradient descent and the gradients are computed by,

$$\nabla_{O_1} f(O_1,O_2,O_3) = \sum_{i=1}^{N} \alpha_i\, \Pi_i^T\, \Pi_i(\alpha_i O_1 + \beta_i O_2 + \gamma_i O_3)$$

$$\nabla_{O_2} f(O_1,O_2,O_3) = \sum_{i=1}^{N} \beta_i\, \Pi_i^T\, \Pi_i(\alpha_i O_1 + \beta_i O_2 + \gamma_i O_3) \quad . \qquad (6)$$

$$\nabla_{O_3} f(O_1,O_2,O_3) = \sum_{i=1}^{N} \gamma_i\, \Pi_i^T\, \Pi_i(\alpha_i O_1 + \beta_i O_2 + \gamma_i O_3)$$

The $(j+1)^{th}$ iteration of the algorithm is updated as,

$$O_1^{j+1} = O_1^j - t\,\nabla_{O_1} f(O_1,O_2,O_3) = O_1^j - t \sum_{i=1}^{N} \alpha_i\, \Pi_i^T\, \Pi_i(\alpha_i O_1^j + \beta_i O_2^j + \gamma_i O_3^j)$$

$$O_2^{j+1} = O_2^j - t\,\nabla_{O_2} f(O_1,O_2,O_3) = O_2^j - t \sum_{i=1}^{N} \beta_i\, \Pi_i^T\, \Pi_i(\alpha_i O_1^j + \beta_i O_2^j + \gamma_i O_3^j) \quad , \qquad (7)$$

$$O_3^{j+1} = O_3^j - t\,\nabla_{O_3} f(O_1,O_2,O_3) = O_3^j - t \sum_{i=1}^{N} \gamma_i\, \Pi_i^T\, \Pi_i(\alpha_i O_1^j + \beta_i O_2^j + \gamma_i O_3^j)$$

where t is the step size. For a given tilt angle set $\{\phi_i, \theta_i, \psi_i\}$, the forward projection of a 3D object is computed using the Fourier slice theorem, while the back projection is implemented by linear interpolation.

To validate the vector tomography reconstruction algorithm, we simulated 3D topological magnetic monopoles and calculated their diffraction patterns based on the experimental parameters. After adding noise to the diffraction patterns, we performed ptychographic reconstructions to generate projections. Using the vector tomography reconstruction algorithm, we were able to reconstruct the 3D magnetization vector field of the topological monopoles from the projections. After validating the vector tomography algorithm using simulated data, we applied it to reconstruct the 3D magnetization vector field of the ferromagnetic meta-lattice from the experimentally measured tilt series.

Quantification of the 3D spatial resolution. We quantified the spatial resolution using two independent methods. First, we divided the 91 projections of three tilt series into two halves by choosing alternate projections and conducted two independent 3D scalar reconstructions, from which two different supports were generated to separate the nickel from the silica region. We then performed two independent vector reconstructions from the two halves. After applying the support to exclude the silica region, we calculated the Fourier shell correlation (FSC) from the two 3D vector reconstructions. Extended Data Fig. 7a-f shows the FSC for $|m_x|$, $|m_y|$, $|m_z|$, $|m_{xy}|$, $|m_{xz}|$ and $|m_{yz}|$, respectively, where m_x, m_y, and m_z are the *x*-, *y*-, and *z*-component of the unnormalized magnetization vector field and $|m_{xy}| = \sqrt{m_x^2 + m_y^2}$, $|m_{xz}| = \sqrt{m_x^2 + m_z^2}$ and $|m_{yz}| = \sqrt{m_y^2 + m_z^2}$. As m_x, m_y, and m_z have both positive and negative values (Supplementary Video 1), their Fourier coefficients in some resolution shells have small values. To avoid dividing by small values, we computed the FSC for the magnitude of m_x, m_y and m_z. According to the cut-off of FSC = 0.143, a criterion commonly used in cryo-electron microscopy[46], we characterized the 3D spatial resolution of the vector reconstruction to be 10 nm. We noted that the FSC values for $|m_z|$ are slightly smaller than 0.143 at some high spatial frequency (Extended Data Fig. 7c). This was because only a half of the projections were used to perform each 3D vector reconstruction. Compared to cryo-electron microscopy that employs a large number of images for a 3D recosntruction[46], the number of projections in our experiment is much smaller. Thus, when only a half of the projections were used for the vector reconstruction, the spatial resolution was reduced especially along the beam (*z*) direction. Second, we quantified three pairs of topological magnetic monopoles with positive and negative charges distributed along the x-, y- and z-axis in the 3D vector reconstruction (Extended Data Fig. 7g-o). The net topological charge of each monopole pair was calculated to be $Q = 0$, while the topological charge of the positive and negative monopole in each pair was computed to be $Q = +1$ (red dot) and -1 (green dot), respectively. The distance between the red and green dot in each pair is 2 voxels with a voxel size of 5 nm, further demonstrating that a spatial resolution of 10 nm was achieved along the x-, y- and z-axis.

Calculation of the topological magnetic monopole density and charge. We first calculated the topological charge density of every voxel (5×5×5 nm^3) within the bulk of the meta-lattice by discretizing the expression $\rho = \frac{3}{4\pi}\partial_x \boldsymbol{n} \cdot (\partial_y \boldsymbol{n} \times \partial_z \boldsymbol{n})$ on a cubic lattice, producing a 3D map of the local maxima (positive) and minima (negative) of the charge density. At each local extremum, we chose 3×3×3 vectors surrounding the local extremum. To compute the topological charge enclosed by these vectors, we triangulated the surface and calculated the solid angle (ω) of each triangle surface subtended by three vectors ($\boldsymbol{n}_1, \boldsymbol{n}_2, \boldsymbol{n}_3$),

$$\tan\frac{\omega}{2} = \frac{\boldsymbol{n}_1 \cdot (\boldsymbol{n}_2 \times \boldsymbol{n}_3)}{1 + \boldsymbol{n}_1 \cdot \boldsymbol{n}_2 + \boldsymbol{n}_1 \cdot \boldsymbol{n}_3 + \boldsymbol{n}_2 \cdot \boldsymbol{n}_3} \quad . \qquad (8)$$

The topological charge was evaluated by $Q = \frac{1}{4\pi}\sum_{\text{facets}} \omega$, which is an integer as the summation of all solid angles over an enclosed surface is an integer number of 4π. We evaluated the topological charge of the magnetic voids using the same approach.

Atomistic simulations using the experimental data as direct input. Four 15×15×15 nm^3 volumes of the experimentally determined 3D magnetization vector field were extracted from the ferromagnetic meta-lattice as direct input to atomistic simulations. The four volumes contain four topological magnetic monopoles with two positive and two negative charges and each topological magnetic monopole is located close to the centre of each volume. A Ni fcc lattice with a lattice constant of 3.524 Å was constructed for each volume and all atomic sites within each 5×5×5 nm^3 voxel were mapped to the same normalized magnetization vector determined from the experiment, yielding a total of 296,352 atomistic spins in each volume. The dynamics of the individual atomistic spins is described by the Landau-Lifshitz-Gilbert equation of motion[47],

$$\frac{\partial \mathbf{S}_i}{\partial t} = -\frac{\gamma}{\mu(1+\lambda^2)}\left[\mathbf{S}_i \times \mathbf{H}_{\mathrm{eff}}^i + \lambda \mathbf{S}_i \times \left(\mathbf{S}_i \times \mathbf{H}_{\mathrm{eff}}^i\right)\right] \ , \quad (9)$$

where $\mathbf{S}_i$ is a unit vector at atomistic site i, γ is the gyromagnetic ratio, λ is the phenomenological coupling constant (damping) and μ is the magnetic moment. $\mathbf{H}_{\mathrm{eff}}^i$, given by equation (11), is the effective magnetic field at site i. The total energy of the system is represented by the following atomistic spin Hamiltonian,

$$\mathcal{H} = -J\sum_{\langle ij\rangle} \mathbf{S}_i \cdot \mathbf{S}_j - k_u \sum_i (S_i^z)^2 - \mu\, \mathbf{B} \cdot \sum_i \mathbf{S}_i \ , \quad (10)$$

where the first term on the right hand side is the exchange interaction between spins at site i and j, the second is the uniaxial anisotropy term, and the third is the Zeeman term. The exchange constant (J) and the magnetic moment (μ) are 2.757×10^{-21} Joules per link and 0.606 Bohr magnetons, respectively[48]. The anisotropy constant, k_u, and the external field **B** were neglected in the simulations. The above Hamiltonian can be represented as an effective magnetic field for the spin at site i by taking the negative first derivative,

$$\mathbf{H}_{\mathrm{eff}}^i = -\frac{\partial \mathcal{H}}{\partial \mathbf{S}_i} \ . \quad (11)$$

Based on these equations, we performed atomistic simulations of each volume by fixing the spins on the outer boundary of the volume. All the other spins were allowed to relax to an equilibrium configuration. After 50 ps, a stable magnetic monopole formed in each volume with a topological charge matching the experimental value (Extended Data Fig. 9a-d). Further simulations showed that if the atomistic spins on the outer boundary were fixed, any random spin configuration within each volume yielded identical results. We also conducted atomistic simulations to determine how much of the boundary can be relaxed before each topological magnetic monopole becomes unstable. We found that as long as the atomistic spins were fixed on four of the six surfaces of each volume, the topological magnetic monopole remained stable inside the volume (Extended Data Fig. 9e-h). All these atomistic simulation results confirm that surface constraints can stabilize topological magnetic monopoles.

Data availability

All the experimental data are available at https://doi.org/10.5281/zenodo.5450910.

Code availability

The MATLAB source codes for the scalar and vector tomography reconstruction algorithms and data analysis used in this work are available at https://doi.org/10.5281/zenodo.5450910.

32. Watanabe, R. *et al.* Extension of size of monodisperse silica nanospheres and their well-ordered assembly. *J. Colloid Interface Sci.* **360**, 1-7 (2011).
33. Russell, J. L., Noel, G. H., Warren, J. M., Tran, N.-L. L. & Mallouk, T. E. Binary colloidal crystal films grown by vertical evaporation of silica nanoparticle suspensions. *Langmuir* **33**, 10366-10373 (2017).
34. Mahale, P. *et al.* Oxide-Free Three-Dimensional Germanium/Silicon Core-Shell Metalattice Made by High-Pressure Confined Chemical Vapor Deposition. *ACS Nano* **14**, 12810-12818 (2020).
35. Regan, T. J. *et al*. Chemical effects at metal/oxide interfaces studied by x-ray-absorption spectroscopy. *Phys. Rev. B* **64**, 214422 (2001).

36. Lambers, E. C. *et al*. Room-temperature oxidation of Ni(110) at low and atmospheric oxygen pressures. *Oxid. Met*. **45**, 301-321 (1996).
37. Shapiro, D. A. *et al.* An ultrahigh-resolution soft x-ray microscope for quantitative analysis of chemically heterogeneous nanomaterials. *Sci. Adv.* **6**, eabc4904 (2020).
38. Eisebitt, S. *et al.* Lensless imaging of magnetic nanostructures by X-ray spectro-holography. *Nature* **432**, 885–888 (2004).
39. Marchesini, S. *et al.* SHARP: a distributed GPU-based ptychographic solver. *J. Appl. Crystallogr.* **49**, 1245-1252 (2016).
40. Goldstein, R. M., Zebker, H. A. & Werner, C. L. Satellite radar interferometry: Two-dimensional phase unwrapping. *Radio Sci.* **23**, 713–720 (1988).
41. McNaught, A.D. and Wilkinson, A. *Compendium of Chemical Terminology* 2nd edn (Int. Union Pure Appl. Chem., 1997).
42. Yang, Y. *et al.* Determining the three-dimensional atomic structure of an amorphous solid. *Nature* **592**, 60-64 (2021).
43. Hannon, J. P., Trammell, G. T., Blume, M. & Gibbs, D. X-ray resonance exchange scattering. *Phys. Rev. Lett.* **61**, 1245 (1988).
44. Scott, M. C. *et al.* Electron tomography at 2.4-ångström resolution. *Nature* **483**, 444-447 (2012).
45. Pham, M., Yuan, Y., Rana, A., Miao, J. & Osher, S. RESIRE: real space iterative reconstruction engine for Tomography. *arXiv:2004.10445* (2020).
46. Scheres, S. H. W. & Chen, S. Prevention of overfitting in cryo-EM structure determination. *Nat. Methods* **9**, 853-854 (2012).
47. Gilbert, T. L. A phenomenological theory of damping in ferromagnetic materials. *IEEE Trans. Magn*. **40**, 3443-3449 (2004).
48. Evans, R. F. L. *et al*. Atomistic spin model simulations of magnetic nanomaterials. *J. Phys.: Condens. Matter* **26**, 103202 (2014).

Acknowledgements We thank Rafal Dunin-Borkowski and Jong E. Han for stimulating discussions and Yakun Yuan and Yao Yang for help with data analysis. This work was primarily supported by STROBE: a National Science Foundation Science and Technology Center under award DMR1548924. J.M. and A. R. acknowledge support by the US Department of Energy, Office of Science, Basic Energy Sciences, Division of Materials Sciences and Engineering under award number DE-SC0010378 for the development of vector ptychography. J.M. thanks partial support by the Army Research Office MURI program under grant no. W911NF-18-1-0431. M.M. and H.K. acknowledge partial support by the US Department of Energy, Office of Science, Basic Energy Sciences X-Ray Scattering Program Award DE-SC0002002 and DARPA TEE Award No. D18AC00017 for the data acquisition and analysis. Y.T. and J.Z. were supported by the U.S. Department of Energy, Office of Basic Energy Sciences under Grant No. DE-SC0012190. Soft x-ray ptychography experiments were performed at COSMIC used resources of the Advanced Light Source, which is a DOE Office of Science User Facility under contract no. DE-AC02- 05CH11231.

Author contributions J.M. directed the project; M.M.M. suggested the sample; A.J.G, J.V.B, P.M., T.E.M., C.-T.L. and S.Y. synthesized and fabricated the sample; A.R., C.-T.L., Y.H.L., E.E.C.S., S.R., X.L., C.S.B., R.M.K., A.J.G., J.R., H.O., Y.S.Y., D.A.S, H.C.K., M.M.M. and J.M. planed and/or performed the experiments; M.P., A.R., S.J.O. and J.M. developed the scalar and vector tomography algorithms; A.R. and J.M. reconstructed the 3D magnetization vector field; A.R., E.I. J.Z., X.L. and J.M. analysed the data with input from M.M.M., Y.T., C.-T.L., W.L. and V.H.C.; J.H., T.O., E.I. and J.M. discussed and/or conducted the atomistic simulations; A.R., J.M., E.I. and J.Z. wrote the manuscript with input from M.M.M., Y.T., C.-T.L., S.Y., E.E.C.S. and T.E.M.

Competing interests The authors declare no competing interests.

Correspondence and requests for materials should be addressed to J.M. (miao@physics.ucla.edu).

Supplementary Files

This is a list of supplementary files associated with this preprint. Click to download.

- NatureNanoMonopolesExtendedDatafinal.docx
- Video2.mp4
- Video1.mp4